






Comparative study of autofluorescence in flat and tapered optical fibers towards application in depth-resolved fluorescence lifetime photometry in brain tissue

MARCO BIANCO,^{1,2,*}  ANTONIO BALENA,^{1,2}  MARCO PISANELLO,¹  FILIPPO PISANO,¹  LEONARDO SILEO,¹ BARBARA SPAGNOLO,¹ CINZIA MONTINARO,^{1,3} BERNARDO L. SABATINI,⁴ MASSIMO DE VITTORIO,^{1,2,5} AND FERRUCCIO PISANELLO^{1,6} 

¹Istituto Italiano di Tecnologia (IIT), Center for Biomolecular Nanotechnologies, Via Barsanti 14, 73010 Arnesano (Lecce), Italy

²Dipartimento di Ingegneria dell'Innovazione, Università del Salento, Via per Monteroni, 73100 Lecce, Italy

³Dipartimento di Scienze e Tecnologie Biologiche e Ambientali, Università del Salento, Via per Monteroni, 73100 Lecce, Italy

⁴Howard Hughes Medical Institute, Department of Neurobiology, Harvard Medical School, Boston, MA 02115, USA

⁵massimo.devittorio@iit.it

⁶ferruccio.pisanello@iit.it

*marco.bianco@iit.it

Abstract: As the scientific community seeks efficient optical neural interfaces with sub-cortical structures of the mouse brain, a wide set of technologies and methods is being developed to monitor cellular events through fluorescence signals generated by genetically encoded molecules. Among these technologies, tapered optical fibers (TFs) take advantage of the modal properties of narrowing waveguides to enable both depth-resolved and wide-volume light collection from scattering tissue, with minimized invasiveness with respect to standard flat fiber stubs (FFs). However, light guided in patch cords as well as in FFs and TFs can result in autofluorescence (AF) signal, which can act as a source of time-variable noise and limit their application to probe fluorescence lifetime *in vivo*. In this work, we compare the AF signal of FFs and TFs, highlighting the influence of the cladding composition on AF generation. We show that the autofluorescence signal generated in TFs has a peculiar coupling pattern with guided modes, and that far-field detection can be exploited to separate functional fluorescence from AF. On these bases, we provide evidence that TFs can be employed to implement *depth-resolved fluorescence lifetime photometry*, potentially enabling the extraction of a new set of information from deep brain regions, as time-correlating single photon counting starts to be applied in freely-moving animals to monitor the intracellular biochemical state of neurons.

© 2021 Optical Society of America under the terms of the [OSA Open Access Publishing Agreement](#)

1. Introduction

The advent of optogenetics and genetically-encoded fluorescent indicators (GEIs) of neural activity has enabled new types of investigations on causal connectivity in the mammalian brain, as they allow for cell-type specific fluorescent monitoring of intracellular calcium gradients [1], membrane potential [2] and transients of neurotransmitters concentrations [3]. This, in turn, boosted the technological development of implantable photonic devices able to simultaneously deliver and collect light from the living tissue, with the goal of better accessing sub-cortical structures of the mouse brain. In addition, a recent work has highlighted the potential of

Time Correlated Single Photon Counting (TCSPC) techniques to implement Fluorescence Lifetime Photometry (FLiP) and monitor the intracellular biochemical states of neurons through fluorescence reporters in freely-moving animals [4], further extending the set of physiological phenomena that can be probed by functional fluorescence. This has raised the demand for sub-cortical neural interfaces capable of performing FLiP over multiple position across large brain volumes. However, traditional probes such as flat cleaved fiber optics (FFs) fall short in this challenge as they can only interface with a limited volume of tissue near the fiber facet [5,6]. At the same time, opto-electronic (OE) systems with a sub-dermally implanted radiofrequency antenna [7] are limited to a single detection/excitation point and are not compatible with TCSPC. A complementary approach to implantable OE is based on exploiting modal properties of tapered optical fibers (TFs) to readout optical signals with depth resolution [8]. The peculiar geometrical shape of TFs offers a reduced cross-section with respect to standard flat-cleaved fibers (FFs) [9], and can provide either wide-volume or site selective light collection by exploiting the intrinsic mode-division multiplexing and demultiplexing properties of the fiber taper [10], along with the micro-structuring of the taper surface [11–14]. However, light guided in an optical fiber generates an autofluorescence (AF) signal due to the interaction of the travelling light with residual photoactive compounds inside the waveguide. AF reduces the dynamical range of photometry experiments, spectrally overlaps with the collected signal from GFP-based GEIs, alters lifetime detection in FLiP, and can act as a non-constant noise source since the photoactive compounds can bleach over time.

Here we present a comparative study of AF properties of flat and tapered optical fibers typically employed in fiber photometry experiments, showing how the cladding compositions plays a key role in the generation of this spurious signal. On the base of AF intensity, spectral features and its coupling to guided modes detected by far-field detection (FFD), we propose TFs as a suitable system to implement *Depth-Resolved Fluorescence Lifetime Photometry* (DR-FLiP). Although TFs' AF spectrally overlaps with the emission from GFP-based GEIs, we devised a proof-of-concept experiment in brain slices that shows the suitability of TFs to detect fluorescence lifetime signals with depth-resolution using FFD to segregate functional fluorescence from the AF noise.

2. Results

The ability of TFs to collect light from scattering tissue with depth-resolution is enabled by the mode-division multiplexing/demultiplexing properties induced by a narrowing waveguide [8], which can be exploited to generate and collect fluorescence at specific sections of the taper. This is obtained by selecting the input angle of fluorescence excitation light into the fiber, therefore controlling the modal content injected into the waveguide. However, excitation light can generate fluorescence not only from the surrounding medium, but also from the fiber itself, affecting intensity, spectral, lifetime and far-field information employed to study functional fluorescence. In the following, we characterize TFs' AF signals and we compare them with the signal generated by standard FFs. This section is structured as follows: first, we describe the implemented setup to perform intensity, spectral and far-field analysis of the collected signal; *Paragraph 2.2* focuses on the comparison of AF intensity of FFs stubs and TFs realized starting from core/cladding silica/silica or silica/polymer fibers obtained by different suppliers. Then, in *Paragraph 2.3* we study the far-field pattern of the AF signal in order to extract its transversal wave-vector k_t and compare it with the wave-vector injected into the fiber, $k_{t,in}$. Lastly, in *Paragraph 2.4*, we devise a setup to perform depth-resolved fluorescence lifetime photometry, and we show the extracted lifetimes of both AF signal and fluorescence signal collected in *ex vivo* brain tissue.

2.1. Theoretical background and optical setup

Since AF generated by TFs implants for fiber photometry can influence intensity, spectral distribution and far-field patterns of collected functional fluorescence, we used the optical setup displayed in Fig. 1(a) to characterize its properties (see *Materials and methods* for detailed description). A Galvanometric Mirror (GM) allow scanning the input angle of a continuous wave laser beam, to deliver light at different taper sections. Fluorescence light collected from the fiber under test is directed toward intensity, spectral and far-field detectors through a Dichroic Mirror (DM). We tested different fibers with similar NA and a silica core, supplied by different manufacturers: sample 1 (S1) NA 0.39, S2 NA 0.37, S3 NA 0.39, all having polymeric cladding, and S4 0.22 NA featuring a silica cladding (see Table 3 in *Materials and Methods*). For each fiber type, AF was measured in three different device configurations, sketched in Fig. 1(b): a 2m-long patch cord (PC), a PC butt-coupled to a 2 cm-long Flat Fiber stub (PC + FF), a PC butt-coupled to a Tapered Fiber (PC + TF). The setup allows choosing three different detection systems: intensity detection (to study AF relative intensity as a function of θ_{in}), a spectrometer (to identify any difference in AF spectrum on the input angle or across samples) and a far-field imaging path, to analyze intensity distribution in the k_t space of AF signal vs fluorescence collected from the environment.

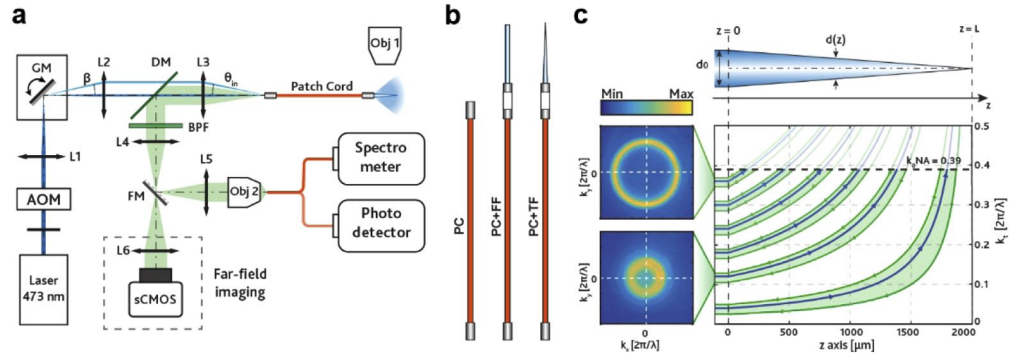


Fig. 1. (a) Setup used for the injection of the light in the fiber, the measurement of the AF signal and for the collection of the far-field pattern. (b) Sketch for the PC, PC + FF, PC + TF configurations. (c) (*top*) Schematic representation of a tapered optical fiber, (*bottom*) evolution of the transverse propagation constant k_t as a function of the taper axis z . Blue lines represent k_t from $0.06 \cdot 2\pi/\lambda$ to $0.36 \cdot 2\pi/\lambda$ with a step of $0.06 \cdot 2\pi/\lambda$. Green lines illustrate the light collected from the TF, with a typical far-field pattern.

As known from the literature [15], increasing input angles θ_{in} leads to modes with higher transversal component of the wave-vector $k_t(z=0)$ to enter the taper. Given an optical fiber with initial diameter d_0 , and a narrowing diameter $d(z)$ along its axis z , the transversal component of the wave-vector of guided modes into the taper is described by the relation

$$k_t(z) = \frac{d_0}{d(z)} \cdot k_t(z=0) \quad (1)$$

whose behaviour is shown by blue lines in the graph in Fig. 1(c). The higher the value of $k_t(z=0)$, the higher the taper diameter at which $k_t(z)$ overtakes the maximum allowed value $k_{t,max} = k_0 NA = 2\pi\lambda^{-1} NA$, generating radiation into the environment at a section z that depends on θ_{in} . When the TF is inserted in a fluorescent medium, emitted radiation generates fluorescence, which is recollected by the TF. Equation (1) applies again for collected light, but in reverse: as light travels toward the patch fiber its k_t decreases, but remains higher for light entering at taper

sections with a higher diameter, as shown by the green lines in the graph in Fig. 1(c). This results in the far-field patterns shown in Fig. 1(c) (*left*), with rings of increasing diameter as θ_{in} increases.

2.2. Autofluorescence intensity and spectral behavior as a function of θ_{in}

We investigated the AF in TFs fabricated starting from step-index optical fibers with similar numerical apertures (NA) and core/cladding diameters. The tapered shape was obtained by heat-and-pull method, with the full procedure described in ref. [16]. Measurements of AF power and spectrum were performed by fixing an output power density from the TF and FF of $\rho_P = 0.1 \text{ mW/mm}^2$ (see Section 4: *Materials and Methods* for details on the power density estimation). Representative AF intensity data as a function of θ_{in} for the fibers with polymeric cladding (S1, S2, S3) are displayed in Fig. 2(a)-(c) (*top*) in the PC, PC + FF and PC + TF configurations (more data for $n=3$ fibers of the same type are reported in *Supplementary Figure 1* in *Supplement 1*). Detected AF power in the PC configuration ranges from 10^{-14} W to 10^{-13} W, and increases as a function of θ_{in} for all samples. PC + FF configuration shows a similar trend, with the AF power being slightly higher, but still in the same order of magnitude. In both PC and PC + FF configurations, as θ_{in} increases the high-order modes injected into the fiber interact more with the interface between the core and cladding of the fiber. This let us suggest that, in polymeric patch cords and flat stubs, most of the AF signal is generated in the cladding. Moreover, we observe that in PC + FF configuration the increase in AF power is not proportional to the increase in length with respect to PC configuration. This may be due to a residual air layer at the ferrules butt coupling: light out-coupling from the core of the patch cord can be coupled to the polymeric cladding of the flat stub, causing an increased AF. In the PC + TF configuration, increased AF signal was observed for all the samples, with detected power in the order of 10^{-12} W for all S1-S3 samples, with no consistent trend as a function of θ_{in} for all the three fibers with polymeric cladding. Although the polymeric cladding in 0.39 NA fibers is not present along the taper [10], during the heat-and-pull the polymer can likely lead to small infiltrations within the core, generating spurious bulk photoactive compounds in the taper volume. To further investigate the effect of the pulling angle ψ on the AF signal, we performed a more detailed analysis for sample S1, acquiring AF power as a function of θ_{in} for TFs with different taper angles. Data are reported in *Supplementary Figure 2* in *Supplement 1*.

Spectral analysis (Fig. 2(a)-(c) *bottom*) confirmed these trends, with a broad distribution of emission spectra in the 500-550 nm range, overlapping the emission of GFP-based GEIs [17,18]. Spectra were acquired with a 1000 ms exposure time and have similar shapes for different θ_{in} , with only S3 showing a slight increase in counts at higher wavelengths, probably due to the different material of S3 fiber (not disclosed by the supplier).

To further investigate the effect of the cladding on the generation of the AF signal, we performed the same analysis of PC, PC + FF and PC + TF made with S4 fiber type, with 0.22 NA and a silica cladding. Due to the different NA, light in the S4 samples can be injected with a maximum angle of $\theta_{Max} = \sin^{-1}(0.22) \cong 12^\circ$. AF power as a function of θ_{in} is reported in Fig. 2(d) (*left*). The interaction of travelling light with the cladding doesn't show a significant effect, as we observed a constant AF signal in the order of 10^{-13} W in PC and PC + FF configuration, as opposed to S1, S2, and S3 samples, where the power increased with θ_{in} . Interestingly, in the PC + TF configuration we measured only a slight increase in AF signal, which remained in the range of 10^{-13} W, in contrast to samples with polymeric cladding which exceeded 10^{-12} W. As observed in Fig. 2(d) (*right*), AF emission is in the same spectral region, overlapping with the emission of GEIs, although with fewer counts than polymeric samples, as spectra for S4 fibers were register with a four-time higher exposure time. We should also note that some of the signal may be generated in the epoxy resin used to connectorize the fibers, since it is characterized by an emission in the same spectral range, as shown in Fig. 2(e). The contribution of the epoxy resin may also explain the slight increase of AF power in PC + FF with respect to PC, since another ferrule is needed in

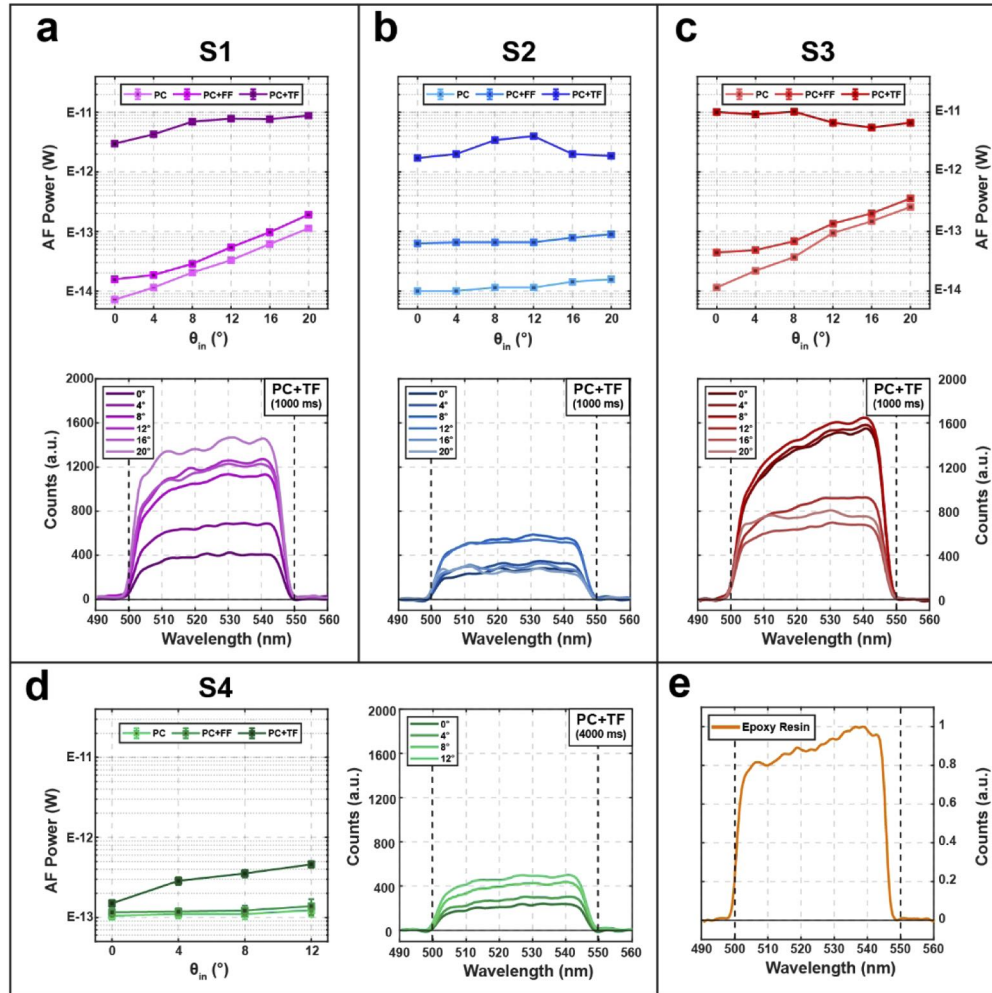


Fig. 2. (a) (*top*) AF power as a function of the input angle θ_{in} for the polymeric cladding S1 fiber type in the PC, PC + FF and PC + TF configurations. Error bars represent the standard deviation of the signal. (*bottom*) AF spectra for different θ_{in} acquired for S1 fiber in the PC + TF configuration (1000 ms exposure time). (b) and (c) show the same plots for, respectively, S2 and S3 polymeric cladding fibers. (d) (*left*) AF power as a function of the input angle θ_{in} for the silica cladding S4 fiber type in the PC, PC + FF and PC + TF configurations. Error bars represent the standard deviation of the signal. (*right*) AF spectra for different θ_{in} acquired for S4 fiber in the PC + TF configuration (4000 ms exposure time). (e) Normalized emission spectrum of the epoxy resin used to connectize both FFs and TFs.

PC + FF configuration. Core/cladding silica/silica TFs revealed almost the same AF intensity of standard flat-cleaved fibers stubs while the polymeric cladding increases AF signal, although this can be partially reduced by photobleaching the fiber, as shown in *Supplementary Figure 3*. In next paragraph we show that this latter can be reduced of about one order of magnitude by employing far-field detection, bringing it to standard FFs values.

2.3. Far-field analysis of collected signal

As shown in Fig. 1(a), to analyze the far-field pattern of detected fluorescence, the collected fluorescence was collimated by lens L3 and sent to a 4f system composed by lenses L4 and L6 to image the far-field pattern on the chip of an sCMOS camera (the reciprocal space is hereafter referred to as (k_x, k_y)). In general, given r the distance from the center of the camera chip of the generic point (k_x, k_y) , the signal detected at r is related to the transversal wave-vector k_t of light re-emitted by the input facet according to the equation [19,20]

$$k_t = \frac{2\pi}{\lambda} \sin \left(\tan^{-1} \left(\frac{f_4}{f_3 f_6} r \right) \right) \quad (2)$$

As shown in Fig. 3(a), the input angle θ_{in} and the injected $k_{t, in}$ are linked by a linear relationship [10], therefore enabling a direct comparison of $k_{t, in}$ with $k_{t, fluo}$, the transversal wave-vector extracted when the TF is in a fluorescent medium.

When the TF is submerged in a fluorescent solution (30 μ M PBS:Fluorescein), light out-coupling from the taper generates fluorescence (Fig. 3(b)) which is collected by the TF itself. The collected far-field patterns have the shape of a ring, whose diameter increases as θ_{in} increases (Fig. 3(c)). Acquired data show that $k_{t, fluo} \leq k_{t, in}$ (see fluorescence signal inside the red ring in Fig. 3(c)), since excitation light emitted in the environment is not orthogonal to the TFs' surface, but is directed toward the tip (Fig. 3(b)). Therefore, fluorescence is collected at slightly lower diameters with respect to the main output position. Figure 3(d) instead shows representative AF far-field data acquired for the PC + TF configuration, with the TFs submerged in a non-fluorescent PBS bath, by injecting light with $\theta_{in} = 0^\circ$ and $\theta_{in} = 12^\circ$, for samples S1, S2 and S3, representing the worst-case conditions with respect to samples S4. At $\theta_{in} = 0^\circ$ we observe a very weak signal for S2 device, while a ring is visible for samples S1 and S3. By injecting light with $\theta_{in} = 12^\circ$ a larger ring is clearly visible for all the samples. Far-field patterns are acquired by setting the exposure time of the camera to 1000 ms. Images in Fig. 3(d) are normalized to their relative maximum, with the total intensity of the frame different for each image. The total counts for the frames showed in Fig. 3(d) are reported in Table 1.

Table 1. Total counts of the far-field images acquired for $\theta_{in} = 0^\circ$ and $\theta_{in} = 12^\circ$, for the different TFs.

		S1 (counts)	S2 (counts)	S3 (counts)
θ_{in}	0°	$2.0 \cdot 10^{10}$	$1.1 \cdot 10^{10}$	$5.7 \cdot 10^{10}$
	12°	$7.3 \cdot 10^{10}$	$2.6 \cdot 10^{10}$	$13 \cdot 10^{10}$

We defined as $k_{t, AF}$ the transversal wave-vector extracted from the AF far-field pattern. Interestingly, in all these cases we found that signal is mostly concentrated at $k_{t, AF} \geq k_{t, in}$. It is possible to evaluate the percentage of the AF signal which is detected at $k_{t, AF} > k_{t, in}$. Figure 3(e) shows radial intensity profiles of far-field images for different θ_{in} values, normalized to their maximum: the dashed vertical line represents the injected $k_{t, in}$ for a given θ_{in} , while the filled area highlights the portion of the recorded signal with $k_{t, AF} > k_{t, in}$. The percentage of the AF signal at $k_{t, AF} > k_{t, in}$ can therefore be estimated and, as displayed in Fig. 3(f), it decreases as a function of θ_{in} , since for increasing angles the distribution of the signal tends to shift toward higher k_t , but a component at lower k_t values remains persistent at all input angles.

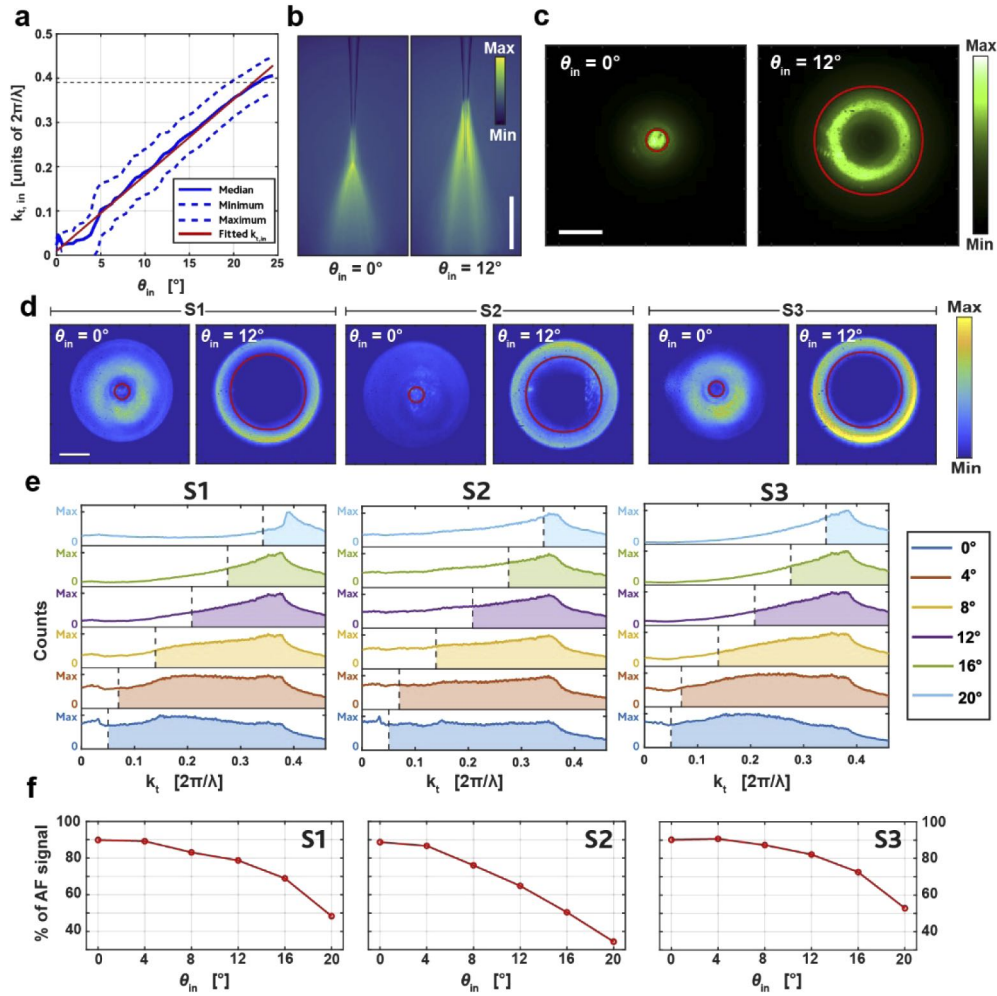


Fig. 3. (a) Plot of $k_{t,in}$ injected into the fiber as a function on the input angle θ_{in} . Solid red line represent the linear fit of the plot. (b) False color fluorescence images showing the emission of light from a TF submerged in a drop of PBS:Fluorescein, for $\theta_{in} = 0^\circ$ and for $\theta_{in} = 12^\circ$. Scale bar represents 500 μm . (c) Corresponding far-field images acquired for the same angles, with the TF submerged in fluorescent solution. The red circle represents the corresponding Median $k_{t,in}$, extracted from panel (a). Scale bar represents $0.2 \cdot 2\pi/\lambda$. As observed, most of the signal is inside the red circle, and $k_{t,fluo} \leq k_{t,in}$. (d) Representative AF far-field pattern, acquired for each sample, with the TF submerged in a non-fluorescent solution, for $\theta_{in} = 0^\circ$ and $\theta_{in} = 12^\circ$. As shown, in this case $k_{t,AF} \geq k_{t,in}$. Scale bar represents $0.2 \cdot 2\pi/\lambda$. Images are normalized to their relative maximum. (e) Normalized radial intensity profile plots for different θ_{in} extracted from the far-field images obtained, for samples S1, S2 and S3. The dashed vertical line represents the injected $k_{t,in}$ for a given θ_{in} , while the filled area represents the portion of AF signal at $k_{t,AF} \geq k_{t,in}$. (f) Percentage of the AF at $k_{t,AF} > k_{t,in}$ as a function of θ_{in} for the three samples.

2.4. Depth-resolved fluorescence lifetime photometry measurements

To evaluate the influence of AF signal on TCSPC performed with TFs we have implemented the setup displayed in Fig. 4(a), allowing for Depth-Resolved Fluorescence Lifetime Photometry (DR-FLiP). A picosecond pulsed laser beam was coupled into the fiber with an angle controlled through a galvanometric mirror, following the same path described in previous paragraphs. Figure 4(b) shows the resulting emission for $\theta_{in} = 0^\circ$ and $\theta_{in} = 20^\circ$ with a TF implanted in a 300 μm thick coronal brain slice from a (Thy1-GCaMP6s) GP4.12Dkim/J mouse, expressing GCaMP in both cortex (L5) and hippocampus (CA1). The fluorescence excited in the tissue is collected back through the TF, re-emitted at the input facet, and sent through the far-field imaging system, where the sCMOS camera was replaced by a 16 channels common anode photomultiplier tube (PMT) for TCSPC measurements. Before performing the DR-FLiP measurements, we verified that the system could properly collect and image the far-field pattern even in a scattering medium. The comparison between the acquisitions performed in PBS:Fluorescein and in a coronal mouse brain slice is reported in *Supplementary Figure 4*. With reference to Fig. 4(b), the two illuminated volumes are approximately spaced 1.1 mm. It is possible to make a qualitative estimation of the number of illuminated neurons relying both on previous works [8] and on the fluorescence images in Fig. 4(b). We can assess an illumination length along the fiber axis of $L \approx 350 \mu\text{m}$ for both θ_{in} . A TF inserted in brain tissue can excite fluorescence for a distance R along the radial direction of about $R \approx 100 \mu\text{m}$ [8]. According to ref. [21], neurons density in the cortex (L5, emission position far from the tip) is $\rho_{L5} = 92000 \text{ cells}/\text{mm}^3$, while in the hippocampus (CA1, emission position near the tip) is $\rho_{CA1} = 65000 \text{ cells}/\text{mm}^3$. The TF's emission volume can be approximated with a hollow cylinder, where the internal radius is the radius of the TF at a given section. The approximate evaluation gives $N_{L5} \approx 6000$ neurons in the cortex, and $N_{CA1} \approx 2000$ neurons in the hippocampus.

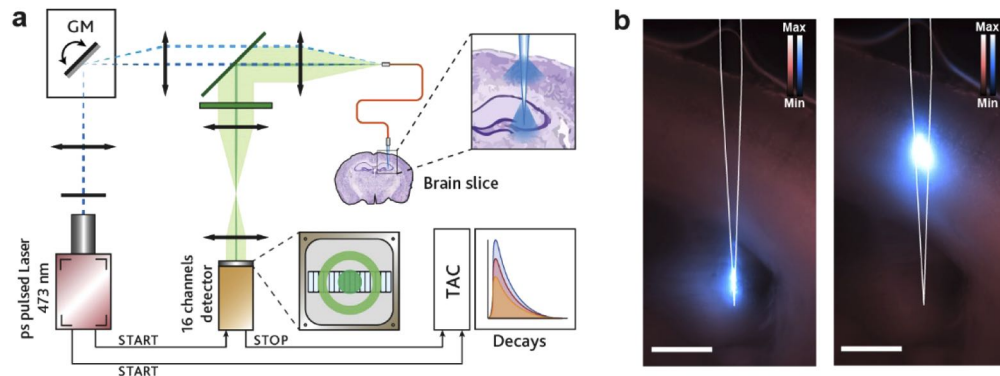


Fig. 4. (a) Sketch of the setup employed for the DR-FLiP measurements. Fluorescence excited in the TF or in the tissue is back-propagated and directed to the FFD path. Light distribution over the linear array depends on θ_{in} . (b) Fluorescence images of the TF inserted into a mouse brain slice. Blue field represent the fluorescence generated by the pulsed laser light emitted by the TF, pink field is the fluorescence of the tissue when excited with a LED source. Scale bar represents 500 μm .

As schematized in Fig. 4(a), for the lower θ_{in} the pattern projected on the array is centered on the central channels of the array, while, for the higher θ_{in} fluorescence intensity is on outer channels. Experimentally, this results in the representative decay curves displayed in Fig. 5 for the two θ_{in} . The decay curves were fitted with a mono-exponential function in order to extract the corresponding lifetime τ (details in Section 4: *Materials and Methods*). In the brain slice, at $\theta_{in} = 0^\circ$ (Fig. 5(a)) central channels (from #6 to #9) show the highest signal, with a decay

time of $\tau_{tissue, 0^\circ} = 1.43 \pm 0.09 \text{ ns}$. At $\theta_{in} = 20^\circ$ (Fig. 5(b)) fluorescence is instead spread on outer channels, but with a similar decay ($\tau_{tissue, 20^\circ} = 1.43 \pm 0.11 \text{ ns}$). The same method was employed to study AF, with the taper outside the brain slice in a non-fluorescent bath, whose behavior is shown in Fig. 5(c,d). For $\theta_{in} = 0^\circ$ an average lifetime among the channels of $\tau_{AF, 0^\circ} = 0.84 \pm 0.03 \text{ ns}$ was recorded, together with a lower overall fluorescence intensity and with slightly higher relative signal on channels #7 and #9, with respect to measurements in tissue for the same input angle, as expected from the far-field analysis of AF described in paragraph 2.3. When $\theta_{in} = 20^\circ$ a longer lifetime was observed ($\tau_{AF, 20^\circ} = 1.18 \pm 0.07 \text{ ns}$), this may be due to the non-uniform distribution of photoactive compounds inside the TF. Additional AF data at the two angles from different TFs of the same material and with similar taper angle are shown in *Supplementary Figure 5*, giving consistent results in terms AF lifetime. On a total of $n = 3$ TFs we obtained the following lifetimes: $\tau_{AF, 0^\circ} = 0.82 \pm 0.03 \text{ ns}$ for $\theta_{in} = 0^\circ$, and $\tau_{AF, 20^\circ} = 1.16 \pm 0.10 \text{ ns}$ for $\theta_{in} = 20^\circ$, in terms of mean value \pm standard deviation.

The numerical results of the fitting are reported in Table 2.

Table 2. Summary of the parameters extracted from the fitting of DR-FLiP data displayed in Fig. 5.

	Channel	a	$b \text{ (ns}^{-1}\text{)}$	M_i	$\tau \text{ (ns)}$	R^2
Tissue $\theta_{in} = 0^\circ$	6	1428	-0.675	1321	1.481	0.994
	7	4406	-0.666	4067	1.501	0.997
	8	4451	-0.772	4047	1.296	0.996
	9	3305	-0.667	3002	1.499	0.996
Tissue $\theta_{in} = 20^\circ$	5	4648	-0.628	4246	1.592	0.996
	6	3831	-0.759	3458	1.317	0.995
	7	2430	-0.709	2116	1.410	0.992
	9	2269	-0.712	2034	1.405	0.993
	10	1736	-0.807	1529	1.239	0.993
	11	4859	-0.699	4342	1.430	0.995
Air $\theta_{in} = 0^\circ$	6	592	-1.150	603	0.870	0.997
	7	2084	-1.178	2145	0.849	0.998
	8	1277	-1.258	1250	0.795	0.998
	9	1916	-1.160	1983	0.862	0.998
Air $\theta_{in} = 20^\circ$	5	1595	-0.799	1585	1.252	0.994
	6	867	-0.949	856	1.054	0.997
	7	672	-0.854	625	1.171	0.996
	11	1270	-0.851	1197	1.176	0.995

The AF decay in Fig. 5(c,d) are representative data, collected on the same fiber used for acquiring the DR-FLiP in Tissue in Fig. 5(a,b), and show that the 16 channels PMT placed in the far-field plane allows spreading part of the AF signal on some channels where the functional fluorescence signal is not present or very low. We have therefore defined the ratio between the Total Fluorescence Signal (TFS) and the AF as a figure of merit to identify the channels less influenced by AF photons. The TFS/AF value for each channel is reported in Fig. 6, with reference to the data shown in Fig. 5, and compared with the same figure of merit measured by summing the data from all channels on the detector, e.g. using it as a standard PMT with only one channel TFS/AF_{total} (horizontal line in the bar graph in Fig. 6). For the lower input angle $TFS/AF > TFS/AF_{total}$ in the central channels of the detector, while in case of the higher input angle $TFS/AF > TFS/AF_{total}$ happens in the external channels. This gives a quantitative estimation of the advantage of using a multichannel PMT placed in the far-field plane. Therefore, if the sCMOS camera using for far-field imaging can be employed to segment the acquired image and partially remove autofluorescence, the multichannel PMT instead increases the ratio between the actual fluorescence signal and the AF counts on specific detection channels.

A comparison experiment was implemented with a FF collecting light from the cortex of a 300 μm -thick coronal brain slice from a (Thy1-GCaMP6s) GP4.12Dkim/J mouse, whose data

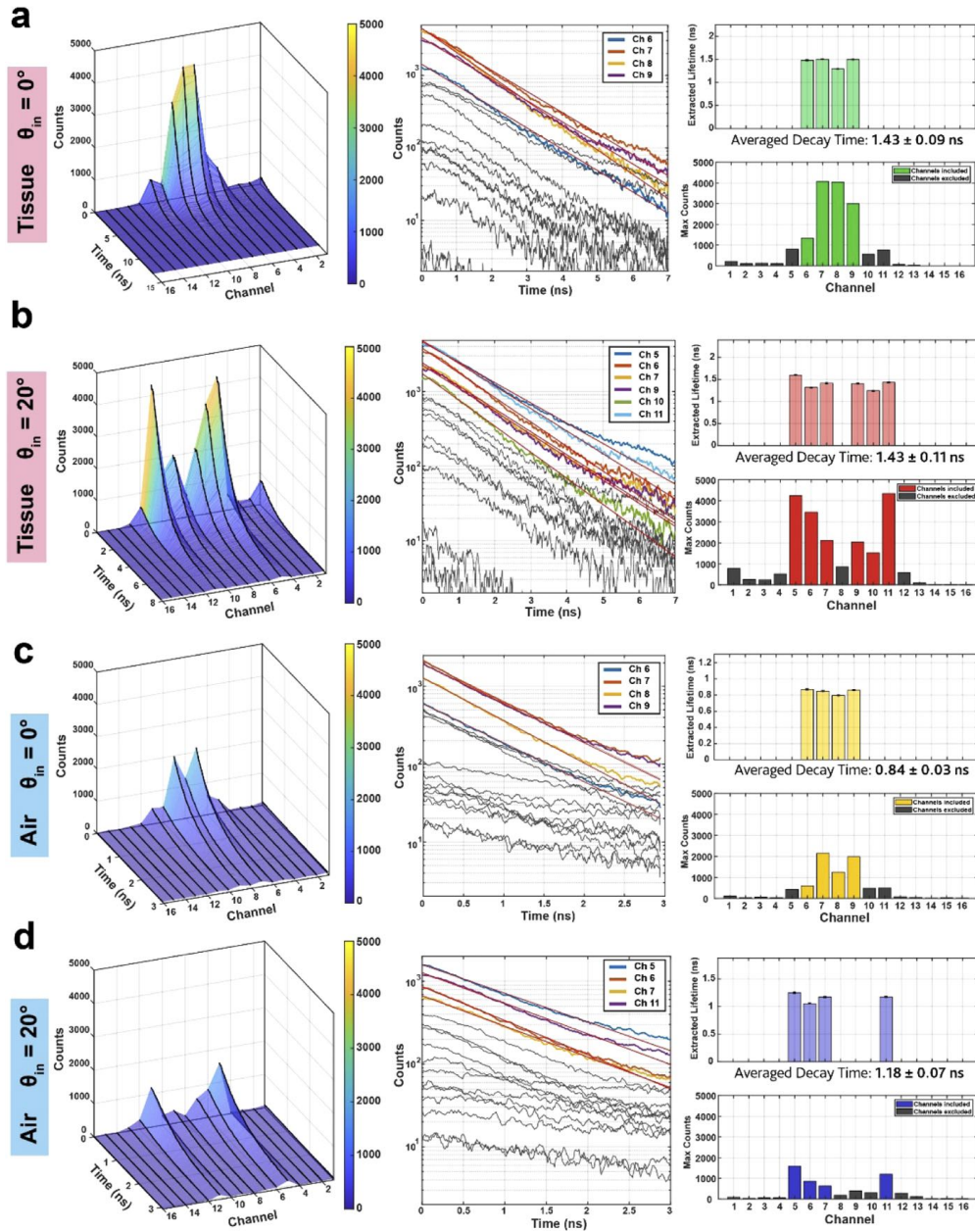


Fig. 5. (a-b) Results of the analysis for DR-FLiP measurements with the TF (Sample S2, taper angle 3.7°) implanted in a $300\ \mu\text{m}$ -thick coronal brain slice from a (Thy1-GCaMP6s) GP4.12Dkim/J mouse, $\theta_{in} = 0^\circ$, and $\theta_{in} = 20^\circ$. *Left* column is the decay map for all the channels of the array. *Center* column shows the results of the fitting for the decay tracks over threshold, logarithmic scale. Tracks under threshold are shown in gray, and are excluded from the evaluation of the lifetime τ . On *right* column are reported the extracted lifetimes, and the maximum counts per channel. (c-d) Same analysis for the AF of the fiber, for $\theta_{in} = 0^\circ$, and $\theta_{in} = 20^\circ$.

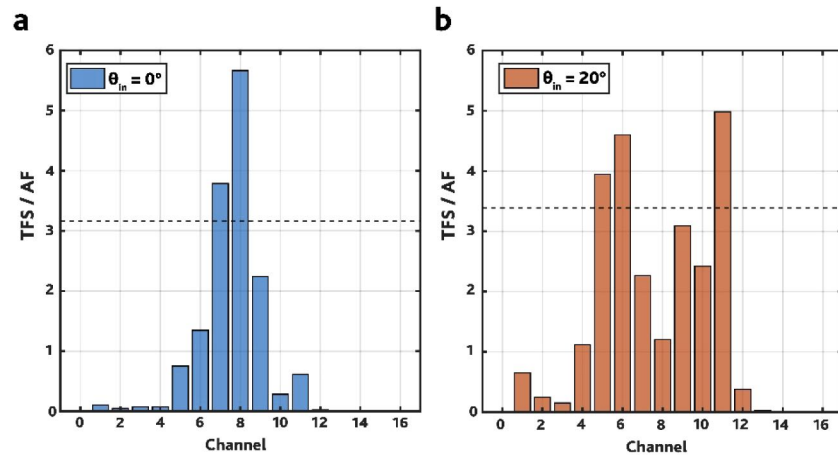


Fig. 6. Bar graph showing the TFS/AF obtained by the ratio of TFS and AF. The evaluation was done for $\theta_{in} = 0^\circ$ (hippocampus, panel *a*) and for $\theta_{in} = 20^\circ$ (cortex, panel *b*). The dashed line represents the same figure of merit when the linear array is used as a standard PMT, i.e. by summing all the counts on the channels.

are reported in Fig. 7. The decay map of the counts is more spread over the detector's channels with respect to the TF, covering the entire fiber NA projected in the far-field plane. The pattern projected on the linear array has a gaussian-like shape (Fig. 7), as expected from the far-field pattern of a FF, with six channels over threshold distributed around the center of the array (#5 to #10), with AF signal below the detection limit. Although TFs introduce a weak AF signal, the spatial differentiation provided by the multichannel detector can be exploited to improve the TFS/AF ratio (Fig. 6). Further data on how AF and TFS compares when related to the far-field multichannel detection for different values of θ_{in} are shown in *Supplementary Figure 6*. When the same brain region is compared, both FFs and TFs give compatible decay times ($\tau_{tissue, FF} = 1.51 \pm 0.12$ ns and $\tau_{tissue, 20^\circ} = 1.43 \pm 0.11$ ns in cortex). However the FF is limited to a single excitation position per implant: the same measurement performed in the hippocampus region would have required another deeper implant, resulting in more damage to the brain tissue. With regard to the AF of the FF, the signal was too noisy to be properly recorded and analyzed.

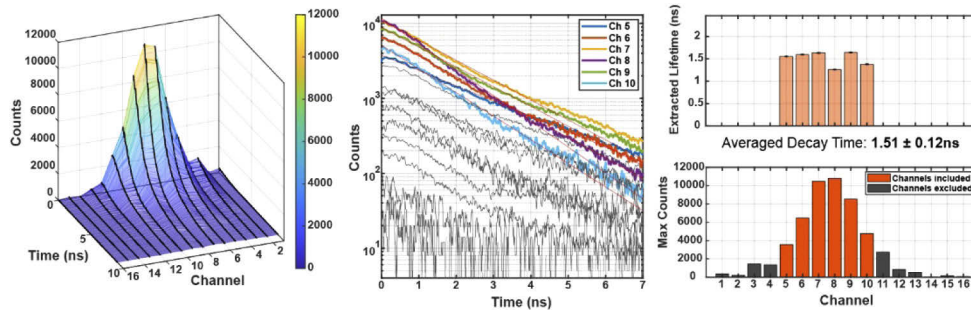


Fig. 7. DR-FLiP measurements with a flat fiber implanted in in the cortex of a 300 μm -thick coronal brain slice from a (Thy1-GCaMP6s) GP4.12Dkim/J mouse. (a) Decay map for all the channels of the array. (b) results of the fitting for the decay tracks over threshold, logarithmic scale. Tracks under threshold are shown in gray, and are excluded from the evaluation of the lifetime τ . (c) extracted lifetimes, and the maximum counts per channel.

3. Discussion and conclusion

As fiber photometry becomes a widely spread technique to monitor neural activity of molecularly-defined cellular populations, new technologies and methods are being proposed to extend its experimental capabilities [22–24]. In this framework, TFs recently enabled the collection of functional fluorescence in a depth-resolved fashion, introducing a new experimental approach to multiplex signals from multiple sub-regions in the same waveguide [8,14]. Here we present a study of autofluorescence (AF) signal generated in TF, analyzing its coupling to guided modes and its time-resolved dynamics.

We have found that AF spectrally overlaps with the emission of GFP-based indicators of neural activity, and that TFs obtained starting from optical fibers with inorganic silica cladding have AF powers comparable to those detected in the case of standard flat-cleaved stubs. On the contrary, polymeric claddings strongly increase AF signal of TFs, whose value can be reduced by means of image segmentation on far-field detection. Indeed, far-field analysis reveals that AF couples to guided modes with higher transversal component of the wave-vector with respect to fluorescence collected from the environment surrounding the taper, independently on the input angle of fluorescence excitation light.

One main advantage of TFs with respect to other technologies is their intrinsic compatibility with TCSPC systems. To enable lifetime measurements resolved in the reciprocal space, we have employed a multi-channel single photon counting detector placed on the fiber's far-field plane, obtaining a partial separation of the autofluorescence signal from the functional fluorescence by virtue of their different distribution in the k_t space. Although autofluorescence from flat-cleaved fibers (FFs) is lower if compared with TFs, this k_t -resolved detection allows for improving the ratio between the overall fluorescence and the autofluorescence signal and introduces the possibility to collect depth-resolved data. This was shown for cortex and hippocampus in coronal sections of *Thy1-GCaMP6s* mice, with the data extracted from cortical layers with TFs resulted to be very close to the one measured with FFs. Lifetime measurements of AF signal in TFs has shown a typical lifetime ~ 1 ns, while fluorescent dyes previously employed for FLiP (for instance based on the ratiometric FRET sensor AKAR3) have longer baseline lifetimes > 2 ns [4,25,26]. Given that with DR-FLiP was possible to estimate a decay time ~ 1.43 ns against an AF lifetime of ~ 0.84 ns, longer lifetimes, like the ones featured by AKAR3, should not pose a challenge to our method. Given that the fluorescence signal distribution in the k_t space is resilient to modal mixing induced by the patch-fiber movements [8], this approach has the potential to be applied in freely-moving animals and could represent an important complement to current FLiP techniques. Implementing in vivo DR-FLiP will however require a scanning system to select the light emission/collection depth, and to take into account that TFs AF intensity depends on the input angle θ_{in} , and a calibration step could be useful before implanting the fiber.

In summary, as FLiP is emerging as a new approach to extend the set of phenomenology that can be probed with implanted waveguides and, exploiting a multi-channel detector, TFs allow to measure the time-resolved decay curve at different depths.

4. Materials and methods

4.1. Fiber fabrication process

We fabricated TFs with slightly different numerical aperture NA and taper angle ψ using three different fiber segment: (i) ThorLabs FT200UMT (S1), (ii) Doric MPF 200/220/900-0.37 (S2), (iii) ThorLabs FT200UMT-Custom (S3), (iv) ThorLabs FG200UEA (S4). S3 segment was made by ThorLabs upon the request of a low AF patch cord fiber for photometry applications with a core of $200 \mu\text{m}$. The tapered shape is obtained by heat-and-pull method through a laser puller, using the same fabrication parameters for every set of samples for a given fiber type (S1, S2, S3 or S4). Overall, the process is very repeatable: when the pulling is done, the instrument

displays the total time required for the pulling; a similar pulling time across different pulls is an indicator of TFs whose geometrical properties are very similar one to the other. The samples were then observed using a stereomicroscope, in order to measure the taper angle ψ . Samples with ψ exceeding a tolerance of $\pm 0.5^\circ$ with respect to the desired angle were discarded. A review of the properties for the three samples is reported in Table 3.

Table 3. Review of the main properties for the three types of TF. The samples feature very similar NA and Core/Cladding dimensions. The different taper angle is due to the heat-and-pull method.

	NA	Core/Cladding	Taper Angle ψ
S1	0.39	200/225 μm	3.30°
S2	0.37	200/220 μm	3.70°
S3	0.39	200/225 μm	4.00°
S4	0.22	200/225 μm	3.00°

Flat fiber stubs were made by cutting a small segment of the corresponding fiber type. TFs and FFs were made about 2 cm long. The samples were connectorized with a 1.25 mm stainless steel ferrule using an epoxy resin; then the flat end of every sample is polished to obtain an optimal coupling with the patch cord facet.

Three 2 m long patch cords, one for each of the three different fiber types, were terminated with a SMA connector and a 1.25 mm metallic ferrule. Patch cords, FFs, and TFs connectors were polished to obtain optimal coupling.

4.2. Optical setup specifications

The setup used to optically characterize the AF is composed of different optical paths for the conditioning of the laser beam, the injection of the light into the fiber, the measurement of the AF signal spectrum and intensity, and the imaging of the far-field pattern re-emitted by the fiber. With reference to Fig. 1(a), light source is provided by a 473 nm continuous wave laser (Laser Quantum Ciel), an acousto-optic modulator (AA Opto-Electronic MT80-A1.5-VIS) is used to control the laser power, lens L1 (ThorLabs LA1509-A, $f_1 = 100 \text{ mm}$) focuses the light on the galvanometric mirror (Cambridge Technology 6215H 5mm). The reflected beam is collimated by L2 (ThorLabs AL50100-A, $f_2 = 100 \text{ mm}$), and focused with an angle θ_{in} to the facet of the patch cord by L3 (ThorLabs AL4532-A, aspherical, $f_3 = 32 \text{ mm}$). θ_{in} depends on the deflection angle $\beta = \alpha V_{GM}$ of the GM, with V_{GM} being the GM driving voltage and α a proportionality factor, which defines the beam position at the input of L3. The input angle θ_{in} as a function of V_{GM} can be obtained by the following empiric relation

$$\theta_{in} = \tan^{-1} \left[\frac{f_2}{f_3} \tan \beta \right] \cong CV_{GM} \quad (3)$$

with $C = 4^\circ/V$.

Light guided inside the patch cord couples to the fiber optics under test by a ferrule-to-ferrule junction, and it is out-coupled at the distal end of the device. The same device collects generated fluorescence, which travels back into the patch cord and is collected by lens L3. Light is then reflected by a dichroic mirror (DM, ThorLabs DMSP490L), and filtered by a band pass filter (BPF, ThorLabs MF525-39) then focused on the surface of a flip mirror (FM) by lens L4 (ThorLabs LA1301, $f_4 = 250 \text{ mm}$). Light is collimated by lens L5 (ThorLabs LA1027-A, $f_5 = 100 \text{ mm}$) in order to fill the back focal plane of objective Obj 2 (Olympus Plan N 40x 0.65 NA RMS40X) which focuses light inside a patch cord connected to a spectrometer (BroLight BIM-6002A-0005) or to a photodetector (New Focus Visible & IR femtoWatt photoreceiver 2151).

The detection of the far-field pattern was experimentally performed by a far-field imaging system composed by a band pass filter (BPF, 500-550 nm), lenses L4 and L6 (LA1050-N-BK7,

$f_6 = 100 \text{ mm}$), and a scientific Complementary Metal–Oxide–Semiconductor (sCMOS) camera (Hamamatsu C11440 Orca Flash 4.0, 2048×2048 pixels). Together with the two additional detection paths to gather intensity and spectral behavior of the signal, the employed setup allows getting an extensive optical picture of the collected light. By substituting the fluorescent medium around the TF with non-fluorescent phosphate saline buffer (PBS), this method is hereafter employed to study AF behavior generated by TFs and to compare the obtained data with those from standard FFs.

4.3. Power density measurements

The AF measurements were taken by setting the power density ρ_P out-coupling from the device at a fixed value of $\rho_P = 0.1 \text{ mW/mm}^2$. In the PC and PC + FF configuration, the evaluation of ρ_P is straightforward, and is obtained according to

$$\rho_P = \frac{P}{\pi \left(\frac{d}{2}\right)^2} \quad (4)$$

where d is the core diameter and P is the total power out-coupled from the device, measured with a power meter (ThorLabs PM100). By varying the output power of the device using the AOM, is possible to set the power density to the desired value.

For the PC + TF configuration the evaluation of ρ_P is more complex, since TFs out-couple light only from a fraction of the conical surface depending on the input angle of the injected light; therefore, the power density $\rho_P(z)$ is a function of the distance from the tip.

The TF is submerged in a drop of PBS:Fluorescein solution ($30 \mu\text{M}$). Light outcoupled from the fiber excites fluorescence from the solution that is collected by a 4x 0.28NA Objective (Obj 1, Olympus XFLuor 4x/340) and observed through a sCMOS Camera (Hamamatsu C11440 Orca Flash 4.0).

We acquired the images of the TF emission (Fig. 8(a)) varying V_{GM} from 0 V to 5 V with a step of 1 V, which correspond to an angular range of θ_{in} from 0° to 20° with respect to the fiber axis. For every acquired image we extracted the emission profile $p(z)$ (Fig. 8(b)) using ImageJ software.

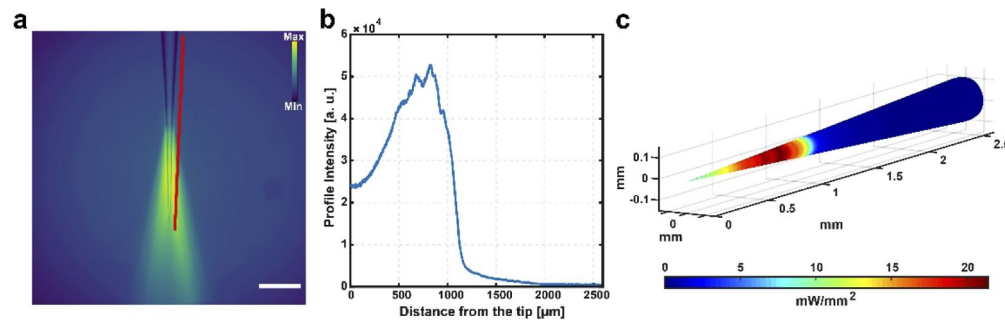


Fig. 8. (a) False color image showing the emission of light from the TF by feeding the GM with a voltage $V_{GM} = 3\text{V}$, corresponding to $\theta_{in} = 12^\circ$. The intensity profile was extracted along a line parallel to the TF surface (red line). Scale bar is $500 \mu\text{m}$. (b) Intensity profile $p(z)$ as a function of the distance from the tip. (c) Results of the evaluation of the power density $\rho_P(z)$ outcoupled from the S2 PC + TF device when light is injected with $\theta_{in} = 12^\circ$, measured output power $P = 2.83\text{mW}$.

Knowing the emission profile $p(z)$ is possible to measure the power density $\rho_P(z)$ of the TF for the corresponding input angle. Assuming a cylindrical coordinate system (r, φ, z) with the

tip of the fiber in the origin and the fiber axis coincident with the z axis of the system, the total output power P emitted from the taper is given by

$$P = \int_{\Sigma} \rho_P(r, \varphi, z) d\Sigma \quad (5)$$

where Σ represents the taper surface. Assuming a cylindrical symmetry, it follows that

$$P = 2\pi \tan\left(\frac{\psi}{2}\right) \left[\cos\left(\frac{\psi}{2}\right)\right]^{-1} \int_0^L z \rho_P(z) dz \quad (6)$$

Since the integral in Eq. (6) can be numerically evaluated starting from the normalized intensity profile $p_{norm}(z)$, the power density distribution of the conical surface can be obtained as

$$\rho_P(z) = \frac{P}{2\pi} \left[\int_0^L z p_{norm}(z) dz\right]^{-1} \cos\left(\frac{\psi}{2}\right) \left[\tan\left(\frac{\psi}{2}\right)\right]^{-1} p_{norm}(z) \quad (7)$$

The evaluation is done with a MATLAB code for every scanning angle, and for every fiber type.

Figure 8(c) shows the result of a simulation for a S2 TF with $0.37 NA$, $\psi = 3.70^\circ$, $V_{GM} = 3 V$ and a measured output power $P = 2.83 mW$.

By averaging $\rho_P(z)$ over the TF surface we get an estimation of the power density ρ_P .

Since the total output power P is proportional to ρ_P , by adjusting P with the AOM is possible to obtain the desired $\rho_P = 0.1 mW/mm^2$ for every input angle θ_{in} .

Between consecutive connections of the same fiber we verified that the output power from the taper was the same for each trial, which assures the same power-transfer efficiency from the patch cord to the taper.

4.4. Analysis of autofluorescence power and spectrum

AF signal was collected as a function of θ_{in} and analyzed in terms of its intensity and spectral distribution.

The power of the AF signal P_{AF} was recorded with a photodetector (PD) sensitive from 1 fW to 0.5 nW, and retrieved by the equation

$$P_{AF} = \frac{V_{AF}}{R \cdot G}, \quad (8)$$

where V_{AF} is the voltage generated by the PD, $G = 2 \times 10^{10} VA^{-1}$ is the PD's gain, $R = 0.35 AW^{-1}$ is the PD's responsivity for $\lambda \cong 525 nm$. V_{AF} was obtained using a DAQ board (National Instruments USB-6363) and LabView code: we measured the average value and the standard deviation of the voltage generated by the PD in a period of 20 s, then subtracted the average value of the noise, measured by turning off the excitation source, in order to retrieve the quantity V_{AF} . The spectra of the AF signal were registered using a fiber-coupled spectrometer, setting the acquisition time to 1000 ms.

Measurement were performed for every fiber type and for each configuration, as a function of the input angle θ_{in} .

4.5. Far-field images processing

In order to extract the transversal wave-vector k_t , a MATLAB code was employed. Starting from the raw image, the algorithm performs a gamma correction to enhance the contrast of the image, then applies a lower threshold to reduce noise, and an upper threshold to remove the residual unfiltered laser light. The code evaluates the centroid of the image, and, starting from this point, an histogram of the counts is retrieved. From the histogram the positions of the minimum (Min), median (Med) and maximum (Max) distance are extracted, then converted in the corresponding k_t values using Eq. (2).

4.6. DR-FLiP setup and methods

For the DR-FLiP we employed a TF, a FF and a patch cord made with S2 fiber type.

The setup for DR-FLiP (Fig. 4(a)) shares most of the optical components with the setup for AF characterization (Fig. 1(a)). The light source employed is a pulsed picosecond 473 nm laser, with pulse rate of 20 kHz, pulse width between 50 ps and 90 ps (Becker & Hickl BDL-SMN) [27]. The detector (Becker & Hickl PML-16 GaAsP) provides 16 simultaneously recording detection channels for TCSPC [27]. The array of detectors contains a multianode photomultiplier tube (PMT) together with 16-channel routing electronics, and the high voltage power supply for the PMT. The distance between the center of the detectors is ~ 1 mm, for a total active length of 16 mm. The detectors and the laser are controlled by a DCC-100 card, which provides for power supply, gain control and overload shutdown. A single photon counting (SPC) module (Becker & Hickl SPC-130EM) contains the TAC/ADC, performs the routing and the recording of the signal, stores the events of the photons detection in registers, and retrieves the histogram of the counts.

The distribution of the light arriving on the array depends from θ_{in} , therefore some channels record mostly noise. Assuming \bar{M} is the maximum count registered by the channels of the array over the period of a measurement, and M_i is the maximum count registered on i -th channel, only the channels where $M_i \geq 0.25 \bar{M}$ were used for the analysis. Decay tracks over the threshold were cleaned from noise and fitted with a mono-exponential function (Eq. (9)) using a MATLAB code, in order to extract the lifetime τ_i of the i -th channel.

$$f_i(x) = a_i \exp(b_i x) \quad \rightarrow \quad \tau_i = -\frac{1}{b_i} \quad (9)$$

The averaged decay time was extracted by evaluating the weighted average in Eq. (10).

$$\tau = \frac{\sum \tau_i M_i}{\sum M_i} \quad (10)$$

Funding. European Commission (828972); National Institutes of Health (1UF1NS108177-01, U01NS094190); European Research Council (677683, 692943).

Acknowledgements. M.B., F. Pisano, A.B., B.S., and F. Pisanello acknowledge funding from the European Research Council under the European Union's Horizon 2020 research and innovation program (#677683). M.D.V. acknowledges funding from the European Research Council under the European Union's Horizon 2020 research and innovation program (#692943). F. Pisanello and M.D.V. acknowledge funding from the European Union's Horizon 2020 research and innovation program under grant agreement No 828972. L.S., M.D.V and B.L.S. are funded by the US National Institutes of Health (U01NS094190). M.P., L.S., F. Pisanello, M.D.V. and B.L.S. are funded by the US National Institutes of Health (1UF1NS108177-01).

Disclosures. L.S., M.D.V., B.L.S. and F. Pisanello are founders and hold private equity in Optogenix, a company that develops, produces and sells technologies to deliver light into the brain. Tapered fibers commercially available from Optogenix were used as tools in the research.

See [Supplement 1](#) for supporting content.

References

1. Y. Yang, N. Liu, Y. He, Y. Liu, L. Ge, L. Zou, S. Song, W. Xiong, and X. Liu, "Improved calcium sensor GCaMP-X overcomes the calcium channel perturbations induced by the calmodulin in GCaMP," *Nat. Commun.* **9**(1), 1504 (2018).
2. K. D. Piatkevich, S. Bensussen, H. Tseng, S. N. Shroff, V. G. Lopez-Huerta, D. Park, E. E. Jung, O. A. Shemesh, C. Straub, H. J. Gritton, M. F. Romano, E. Costa, B. L. Sabatini, Z. Fu, E. S. Boyden, and X. Han, "Population imaging of neural activity in awake behaving mice," *Nature* **574**(7778), 413–417 (2019).
3. T. Patriarchi, J. R. Cho, K. Merten, M. W. Howe, A. Marley, W.-H. Xiong, R. W. Folk, G. J. Broussard, R. Liang, M. J. Jang, H. Zhong, D. Dombeck, M. von Zastrow, A. Nimmerjahn, V. Gradinaru, J. T. Williams, and L. Tian, "Ultrafast neuronal imaging of dopamine dynamics with designed genetically encoded sensors," *Science* **360**(6396), eaat4422 (2018).
4. S. J. Lee, Y. Chen, B. Lodder, and B. L. Sabatini, "Monitoring behaviorally induced biochemical changes using fluorescence lifetime photometry," *Front. Neurosci.* **13**, 766 (2019).

5. M. Pisanello, F. Pisano, M. Hyun, E. Maglie, A. Balena, M. De Vittorio, B. L. Sabatini, and F. Pisanello, "The three-dimensional signal collection field for fiber photometry in brain tissue," *Front. Neurosci.* **13**, 82 (2019).
6. D. C. S. Tai, D. A. Hooks, J. D. Harvey, B. H. Smail, and C. Soeller, "Illumination and fluorescence collection volumes for fiber optic probes in tissue," *J. Biomed. Opt.* **12**(3), 034033 (2007).
7. L. Lu, P. Gutruf, L. Xia, D. L. Bhatti, X. Wang, A. Vazquez-Guardado, X. Ning, X. Shen, T. Sang, R. Ma, G. Pakeltis, G. Sobczak, H. Zhang, D. Seo, M. Xue, L. Yin, D. Chanda, X. Sheng, M. R. Bruchas, and J. A. Rogers, "Wireless optoelectronic photometers for monitoring neuronal dynamics in the deep brain," *Proc. Natl. Acad. Sci.* **115**(7), E1374–E1383 (2018).
8. F. Pisano, M. Pisanello, S. J. Lee, J. Lee, E. Maglie, A. Balena, L. Sileo, B. Spagnolo, M. Bianco, M. Hyun, M. De Vittorio, B. L. Sabatini, and F. Pisanello, "Depth-resolved fiber photometry with a single tapered optical fiber implant," *Nat. Methods* **16**(11), 1185–1192 (2019).
9. F. Pisanello, G. Mandelbaum, M. Pisanello, I. A. Oldenburg, L. Sileo, J. E. Markowitz, R. E. Peterson, A. Della Patria, T. M. Haynes, M. S. Emara, B. Spagnolo, S. R. Datta, M. De Vittorio, and B. L. Sabatini, "Dynamic illumination of spatially restricted or large brain volumes via a single tapered optical fiber," *Nat. Neurosci.* **20**(8), 1180–1188 (2017).
10. M. Pisanello, F. Pisano, L. Sileo, E. Maglie, E. Bellistri, B. Spagnolo, G. Mandelbaum, B. L. Sabatini, M. De Vittorio, and F. Pisanello, "Tailoring light delivery for optogenetics by modal demultiplexing in tapered optical fibers," *Sci. Rep.* **8**(1), 4467 (2018).
11. F. Pisanello, L. Sileo, I. A. Oldenburg, M. Pisanello, L. Martiradonna, J. A. Assad, B. L. Sabatini, and M. De Vittorio, "Multipoint-emitting optical fibers for spatially addressable in vivo optogenetics," *Neuron* **82**(6), 1245–1254 (2014).
12. F. Pisano, M. Pisanello, L. Sileo, A. Quattieri, B. L. Sabatini, M. De Vittorio, and F. Pisanello, "Focused ion beam nanomachining of tapered optical fibers for patterned light delivery," *Microelectron. Eng.* **195**, 41–49 (2018).
13. A. Balena, M. Bianco, M. Pisanello, F. Pisano, L. Sileo, M. De Vittorio, F. Pisanello, and B. Sabatini, "Feedback-assisted femtosecond pulsed laser ablation of non-planar metal surfaces: fabrication of optical apertures on tapered fibers for optical neural interfaces," *Opt. Express* **28**(15), 21368–21381 (2020).
14. E. Maglie, M. Pisanello, F. Pisano, A. Balena, M. Bianco, B. Spagnolo, L. Sileo, B. Sabatini, M. Vittorio, and F. Pisanello, "Ray tracing models for estimating light collection properties of microstructured tapered optical fibers for optical neural interfaces," *Opt. Lett.* **45**(14), 3856–3859 (2020).
15. A. W. Snyder and J. D. Love, *Optical Waveguide Theory* (Springer US, 1984).
16. L. Sileo, M. Pisanello, M. De Vittorio, and F. Pisanello, "Fabrication of multipoint light emitting optical fibers for optogenetics," in Proceedings Volume 9305, *Optical Techniques in Neurosurgery, Neurophotonics, and Optogenetics II*, H. Hirschberg, S. J. Madsen, E. D. Jansen, Q. Luo, S. K. Mohanty, and N. V. Thakor, eds. (SPIE, 2015), p. 93052O.
17. J. Akerboom, T.-W. Chen, T. J. Wardill, L. Tian, J. S. Marvin, S. Mutlu, N. C. Calderon, F. Esposti, B. G. Borghuis, X. R. Sun, A. Gordus, M. B. Orger, R. Portugues, F. Engert, J. J. Macklin, A. Filosa, A. Aggarwal, R. A. Kerr, R. Takagi, S. Kracun, E. Shigetomi, B. S. Khakh, H. Baier, L. Lagnado, S. S.-H. Wang, C. I. Bargmann, B. E. Kimmel, V. Jayaraman, K. Svoboda, D. S. Kim, E. R. Schreier, and L. L. Looger, "Optimization of a GCaMP calcium indicator for neural activity imaging," *J. Neurosci.* **32**(40), 13819–13840 (2012).
18. M. Whitaker, "Genetically encoded probes for measurement of intracellular calcium," *Methods Cell Biol.* **99**, 153–182 (2010).
19. M. Pisanello, A. Della Patria, L. Sileo, B. L. Sabatini, M. De Vittorio, and F. Pisanello, "Modal demultiplexing properties of tapered and nanostructured optical fibers for in vivo optogenetic control of neural activity," *Biomed. Opt. Express* **6**(10), 4014 (2015).
20. A. Della Patria, M. Pisanello, L. Sileo, M. De Vittorio, and F. Pisanello, "Influence of laser beam quality on modal selection in tapered optical fibers for multipoint optogenetic control of neural activity," in *2016 18th International Conference on Transparent Optical Networks (ICTON)* (IEEE, 2016), pp. 1–4.
21. D. Keller, C. Erö, and H. Markram, "Cell densities in the mouse brain: a systematic review," *Front. Neuroanat.* **12**, 83 (2018).
22. H. Adelsberger, O. Garaschuk, and A. Konnerth, "Cortical calcium waves in resting newborn mice," *Nat. Neurosci.* **8**(8), 988–990 (2005).
23. Y. Sych, M. Chernysheva, L. T. Sumanovski, and F. Helmchen, "High-density multi-fiber photometry for studying large-scale brain circuit dynamics," *Nat. Methods* **16**(6), 553–560 (2019).
24. A. Burton, S. N. Obaid, A. Vázquez-Guardado, M. B. Schmit, T. Stuart, L. Cai, Z. Chen, I. Kandela, C. R. Haney, E. A. Waters, H. Cai, J. A. Rogers, L. Lu, and P. Gutruf, "Wireless, battery-free subdermally implantable photometry systems for chronic recording of neural dynamics," *Proc. Natl. Acad. Sci.* **117**(6), 2835–2845 (2020).
25. Y. Chen, J. L. Saulnier, G. Yellen, and B. L. Sabatini, "A PKA activity sensor for quantitative analysis of endogenous GPCR signaling via 2-photon FRET-FLIM imaging," *Front. Pharmacol.* **5**, 56 (2014).
26. G. Cui, S. B. Jun, X. Jin, M. D. Pham, S. S. Vogel, D. M. Lovinger, and R. M. Costa, "Concurrent activation of striatal direct and indirect pathways during action initiation," *Nature* **494**(7436), 238–242 (2013).
27. W. Becker, *The Bh TCSPC Handbook* (2019).